Phase Shift Impact on the performance of Time Modulated Antenna Arrays driven by Radio over Fiber

Phase Shift Impact on the performance of Time Modulated Antenna Arrays driven by Radio over Fiber

A. Giovannini, J. Nanni, L.A. Fernández, G. Paolini, F. Perini, E. Lenzi,
A-L. Billabert, A. Costanzo, J-L. Polleux, D. Masotti, J-M. Laheurte, G. Tartarini

***Abstract*—The joint exploitation of Radio over Fiber (RoF) and Time Modulated Arrays (TMA) is proposed, showing how, particularly within In-Building scenarios, it allows to combine the pervasiveness of the first technique with the beam-steering capability of the second. A cost-effective 3-element RoF-TMA system is presented and investigated, to realize a solution for small offices / private houses (SoHo's). It is confirmed that bringing the feed to the antennas through the RoF system keeps the possibility for the TMA to radiate power at different frequencies, in each case with a steerable maximum direction. Referring to mobile signals with RF carriers of few GHz, it is shown that to guarantee, for each of the multiple beams emitted by the TMA, a maximum deviation of 5° from its ideal direction, it is sufficient that among the output branches of the 1: 3 optical splitter utilized the length difference is maintained in the range of a few millimeters.**

Index Terms—Microwave Antenna Arrays, Optical Waveguides, Radio over Fiber, Time Modulated Arrays

I. Introduction

With the advent of the mobile communication systems of the 5th generation (5G) and of the Internet-of-Things (IoT), a widespread deployment of radiofrequency (RF) systems working from few to tens of GHz is presently taking place [1]. Such high frequency bands have the challenge of the attenuation, which is experienced by signals when they propagate through walls, obstacles and even in free space, increasing with the frequency of the utilized RF carrier [2]. On the other side the decrease of the wavelength makes possible the construction of effective antenna array.

Beamforming Antennas (BAs) are therefore a flexible option which is highly exploited for backhaul application, energy transfer and expected to provide a breakthrough in the pico-cell management [3]. Their steering capabilities and their high directivity offer an additional degree of freedom allowing to selectively direct the RF power to users, on the purpose to transmit data [4] or energy [5].

The technique conventionally utilized to realize BAs consists in obtaining phased arrays through the delicate management of the phase shifts among the radiating elements. The cost is at present rather high, due to the presence of the phase-shifters and the complexity of their design and characterization [6-7]. Conversely, given the necessity to guarantee access to 5G services also in private houses and apartments, the costs of the final global system should be as low as possible. An important challenge is therefore to simplify and compact the architecture of BAs to make them exploitable more massively at lower cost.

These inadequacies can however be overcome utilizing a beamforming technique based on Time Modulated Arrays (TMA) [8]. This technique consists in the time-control of switches placed at each antenna port of the array, instead of using phase-shifters. The periodic piloting of the switches allows the simultaneous availability of multi-harmonic radiation patterns, hence the capability to efficiently send the signal in different directions at the same time. The radiation properties (i.e., the number and the pointing directions of the multiple radiation patterns) are easily reconfigurable in real time by changing the driving waveforms of the switches. Moreover, low-cost is also connected to the use of TMAs, because of their simpler array layout and lower amount of needed components with respect to standard phased-arrays [9]. The challenge of distributing the RF signal into the array is however not modified compared to the phased-array-antennas Within this context, the described advantages can be further enhanced combining TMAs with the Radio over Fiber (RoF) technique, i.e. carrying the RF signals into the arrays through appropriate optical fiber links [10-11].The RoF technique has

This work was supported in part by the "Université Franco Italienne-Università Italo Francese", through the sponsorship of the Joint Doctorate Project C3-2025 "Efficient Wireless Coverage of In-Building Environments with Low Electromagnetic Impact" within the Call Vinci 2019.

A. Giovannini, J. Nanni, L.A. Fernández , G. Paolini, A. Costanzo, D. Masotti and G. Tartarini are with Dipartimento di Ingegneria dell'Energia Elettrica e dell'Informazione "Guglielmo Marconi", Università di Bologna, 40136 Bologna (BO), Italy (e-mail: andrea.giovannini14@unibo.it; jacopo.nanni3@unibo.it;luis.fernandez2@studio.unibo.it;giacomo.paolini4@unibo.it;alessandra.costanzo@unibo.it;diego.masotti@unibo.it;giovanni.tartarini@unibo.it).

F. Perini, is with Institute of Radio Astronomy, National Institute for Astrophysics, Via Fiorentina 3513, 40059 Medicina (BO), Italy (e-mail: f.perini@ira.inaf.it).

E. Lenzi is with Protech S.a.S, Via dei Pini 21, 31033 Castelfranco Veneto (TV), Italy (e-mail: e.lenzi@protechgroup.it).

A.-L. Billabert is with Le Cnam, ESYCOM-CNRS, Paris 75003, France (email:, anne-laure.billabert@lecnam.net).

J. L. Polleux is with Université Gustave-Eiffel, ESYCOM Laboratory, CNRS, ESIEE Paris, Le CNAM, Noisy-le-Grand 93162, France (e-mail:, jean-luc.polleux@esiee.fr).

Jean-Marc Laheurte is with ESYCOM Laboratory, Université Gustave Eiffel, CNRS UMR 9007, France (email: jean-marc.laheurte@univ-eiffel.fr).

indeed been widespread employed for the distribution of radio signals within large beamforming antennas [12] or within Distributed-Antenna-Systems [13]. Depending on the scenario, many consolidated configurations can be utilized, exploiting different kinds of fibers and/or optical sources [14-17].

The present work tackles the realizability of a RoF-TMA system, where the antenna array is reduced to 3-radiating elements to ease the development of a simulation-measurement comparison and to better analyze the key limiting factors of the system, while considering at the same time a possible cost-effective solution for SoHo scenarios. As will be later explained, an important point in the design of these systems is that, in the ideal case, the RoF link should be able to supply each antenna element with exactly the same replica (in amplitude and phase) of the signal to be transmitted. However, while it is easy to have similar excitation amplitudes in the proposed TMA system thanks to the optical fiber low attenuation, it can be challenging to achieve phase-alignment for all antenna currents. The investigation proposed in this work aims at quantifying how these phase shifts influence the Array Factor.

The paper is organized as follows: firstly, the proposed system is described along with an introduction to TMA main theory. Subsequently, a complete analysis of the effects of unwanted phase differences among the signals feeding the three array elements is carried out, allowing to analytically identify acceptable intervals of tolerance for the mentioned phase differences.

Finally, the considerations on the phases impact coming from the simple analytical relations are confirmed through experimental measurements. The generalization to a larger number of elements is then discussed in the conclusive part.

The paper provides also an Appendix section illustrating the derivations of the main theoretical results.

II. Development of the Theoretical Model

The proposed system, shown in Fig. 1 is composed of a Radio over Fiber (RoF) link conveying the signal to a Time Modulated Array (TMA).

In particular, the RoF link includes an Optical Transmitter, modulated by the RF signal to be transmitted, $I_{RF,IN}$,followed by a span of optical fiber. At its terminal section, the fiber is subdivided by an optical splitter into N_a equal optical paths, each one terminating in an Optical Receiver.

Each Optical Receiver is switched on and off, since its control tension V_0 is multiplied by the function $U_n(t)$, with $n = 1, \dots, N_a$, consisting in a periodical sequence of square pulses of period T_M(hence frequency $f_M = 1/T_M$), as depicted in Fig.2. This periodic switching determines in turn a modulation of the feeding current of each antenna of the array, $I_{RF,n}$, with $n = 1, \dots, N_a$. As mentioned in the Introduction, for the correct operation of the TMA both amplitudes $I_{RF,n,MAX}$ and phases ϕ_n of the currents $I_{RF,n}$ should coincide for all n's, the only difference among them being the different modulations due to $U_n(t)$. While the condition can be straightforwardly met for $I_{RF,n,MAX}$ the accomplishment of the condition on the ϕ_n's can be more difficult, e.g. due to slight differences among the lengths of the optical splitter branches.

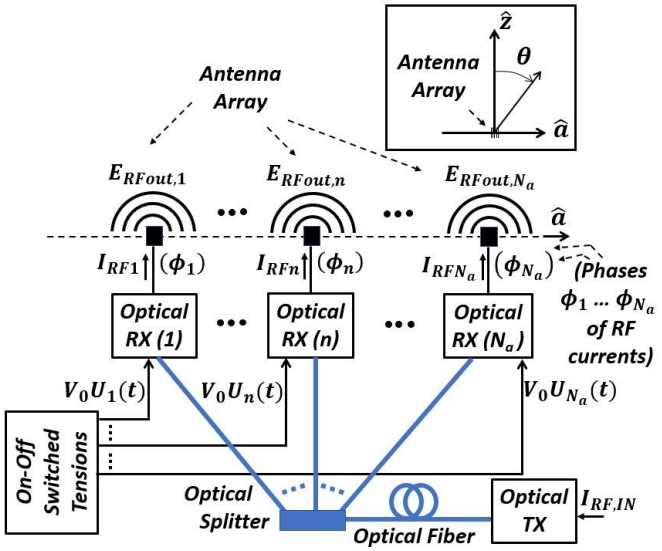

Fig. 1. Schematic of the proposed system resulting from the combination of RoF and TMA technologies. The reference system in the inset shows the angle θ utilized in the representation of the radiation patterns. $I_{RF,IN}$: input RF signal modulating the Optical Transmitter (TX). Letting $n = 1, \dots, N_a$, it is $V_0, U_n(t)$: respectively control tension and modulating sequence of the $n-th$ Optical Receiver (RX(n)); $I_{RF,n}$: input RF signal feeding the $n-th$ antenna, with phase ϕ_n; $E_{RF,out,n}$ electric field radiated by the $n-th$ antenna.

An unpredictable change in the antenna feeding phase is something to be avoided in any kind of radiating system, because this can lead to errors in the beam steering accuracy. In case of planar RF realizations, mechanical tolerances in the feeding lines dimension are in the order of tens of μm, hence with negligible impact on the pointing precision of the beam (e.g., 100 μm change of the length of a 50 Ω line on RF60A Taconic substrate causes 2° of variation of the phase). But even if these tolerances cannot be assured, the deterministic knowledge of the phase misalignment can be compensated in a standard phased-array by properly tune the phase-shifters of each feeding branch. Conversely, in the case of TMAs, this unwanted effect superimposes to the periodic driving sequence effect, i.e., the position of the pulse piloting the generic antenna within the driving period. For this reason, the overall effect is less predictable, and what's more, it is different if the fundamental carrier or one of the available higher order harmonic frequencies is involved.

As mentioned in the Introduction, purpose of this work is to evaluate how these phase shifts influence the Array Factor and this is done for the case of a three-element array. The generalization to a larger number of elements is then discussed in the conclusive part.

It can be noted at this point that within the general scheme of Fig.1, the system can for example be thought as composed by an Optical Transmitter (TX) based on a laser of VCSEL type emitting at 850 nm [18-20], and a corresponding Optical Receiver (RX) based on a Heterojunction Phototransistor (HPTs) realized in SiGe technology. In this case, where V_0 would be the tension between base and emitter of the HPT [21], it would/will be possible to exploit the HPTs' amplifying effect, as well as their perspective integrability with CMOS-process based antennas. Another possible realization of the system of

Fig.1, which will be utilized in the present work, utilizes typical off-the shelf RoF components, namely an Optical TX based on a DFB laser and an Optical RX based on a PIN Photodiode, of which V_0 is the reverse bias tension. Each element of the Antenna Array is then connected to the correspondent photodiode in order to be fed by the RF component of its detected photocurrent.

The time-modulation is responsible for a time-dependency of the array factor as described in (1) for a linear array of N_a elements aligned along $\hat{a}$ (see inset of fig. 1) [22]:

$$AF(\theta,t) = \sum_{h=-\infty}^{+\infty}\sum_{n=1}^{N_a} A_n u_{hn} e^{jkd(n-1)\,sin(\theta)} e^{j2\pi(f_0+hf_M)t} e^{j\phi_n} \quad (1)$$

where $A_n e^{j\phi_n}$ are the complex excitation currents feeding the antennas, k is the wavenumber, d is the antenna spacing. As can be evinced from the formula, the time-periodicity T_M imposed by the impulses $U_n(t)$ allows to Fourier-transform the AF, given by the superposition of harmonics of the array factor itself occurring in correspondence of $f_0 + hf_M$ (where f_0 is the RF carrier frequency, f_M is the modulation frequency, and h is an integer assuming positive and negative values). The coefficients u_{hn} are the complex coefficients of the Fourier transformation of the periodic modulating wave $U_n(t)$.

This phenomenon, peculiar of TMA only, is called "sideband radiation" and was considered a drawback when these radiating systems were presented to the scientific community [8]. More recently, many solutions exploiting this multi-harmonic radiation mechanism have been proposed in the literature: ranging from harmonic beam forming [23], to beam steering [24], and from direction finding [25] to wireless power transfer [22] applications. The novel application envisaged in this paper mainly pertains to improved communication capabilities of existing RoF system: in fact, the almost real time TMA reconfigurability is exploited for simultaneously steering the available radiation patterns at different harmonics to send the modulated signal carrying the data. Note that, being $f_0 \gg f_M$ (i.e., GHz vs. tens/hundred of kHz or few MHz), the antennas are still almost resonating at all these frequencies that indeed represent efficient radiating opportunities.

A key role in the piloting mechanism of TMA is played by the coefficients u_{hn} whose expression, in case of an ideal rectangular pulse as modulating sequence, is usually given in dual form as in [8]. However, it can be demonstrated that these two expressions are actually the same (see Appendix A), leading to the general formula:

$$u_{hn} = c_n sinc(h\pi c_n) e^{-jh\pi(c_n - 2c_{i,n})} \quad (2)$$

In particular, c_n and $c_{i,n}$, being respectively the duty cycle and the rising instant of $U_n(t)$, both normalized to the modulating period (as in Fig. 2), become extremely powerful new design parameters, allowing an almost infinite (especially for large arrays with $N_a \gg 1$) number of possible sequences, and thus an unrevealed level of reconfigurability. Consequently, many sequence optimization strategies have been proposed in the literature [26-28], also taking into account the nonlinear feeding network [29], in order to lead the multi-harmonic radiation to obey to given constraints.

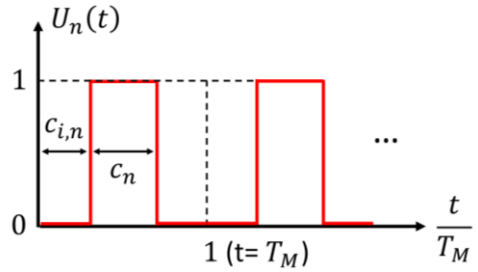

Fig. 2. Generic modulating sequence $U_n(t)$. The square wave oscillates between 0 and 1, has period T_M and is characterized by the duty cycle c_n and the initial delay $c_{i,n}$ (both expressed in percentage of T_M).

For the reasons explained above and for their architectural simplicity (no phase-shifters are needed), TMAs are a potential candidate for future 5G networks agile exploitation.

With the aim to describe theoretically the detrimental effects of undesired phase shifts due to slight differences in length among the branches of the optical splitter, some assumptions will be taken, in order to simplify the analysis of the system considered:

- The duty cycles c_n and the coefficients A_n are constant, so that $c_n = C$ and $A_n = A$.
- The quantities $c_{i,1}$ and ϕ_1 are equal to 0.
- For every frequency of interest $f_0 + hf_M$, in the direction $\theta = \theta_0$, defined as the desired Maximum Radiation Direction (MRD), the complex vectors $u_{hn} e^{jkd(n-1)\,sin(\theta)}$ of the Array Factor have all the same phase for any n.
- The antenna spacing d is equal to $\lambda/2$, so that $kd = \pi$.

The first condition limits the degree of freedom in the selection of the sequence, because forces all the antennas to be "on" for the same amount of the period. At the same time it allows to achieve an analytical formulation of the problem, which can be usefully exploited as a reference case for the study of non-uniform driving sequences. The second condition fixes a zero reference for phase shifts and initial delays, due to the periodic nature of phases and sequences. The third one implies a discrete choice among the $c_{i,n}$ alternatives, hence it imposes a rule similar to the one that the binary optimized time sequences (BOTS) [26] and the sub-sectional optimized time steps (SOTS) [27] methods suggest for TMA time-sequence optimization. Finally, the fourth condition defines a very common antenna spacing.

Given the previous hypotheses, the squared magnitude of the h-th harmonic Array Factor $|AF_h(\theta,t)|^2$, related to the power transmitted by a 3-element TMA to the receiver side, can be deduced from (1) as:

$$\begin{aligned} &|AF_h(\theta,t)|^2 \\ &= |AC\ sinc(h\pi C)|^2 \left| \sum_{n=1}^{3} e^{j((u_{hn}+(n-1)\pi\ sin(\theta)+\phi_n)} \right|^2 \\ &= |AC\ sinc(h\pi C)|^2 \left(3 + 2\Re e\left\{\left(2cos\left(\phi_2 - \frac{\phi_3}{2}\right)\right.\right.\right. \\ &\left.\left.\left. + e^{j\left(\pi\,sin(\theta_0) - \pi\,sin(\theta) - \frac{\phi_3}{2}\right)}\right) e^{j\left(\pi\,sin(\theta_0) - \pi\,sin(\theta) - \frac{\phi_3}{2}\right)}\right\}\right) \end{aligned} \quad (3)$$

where the last member of the equation is obtained by exploiting both the property in (11) of the Appendix C and the phase alignment of the vectors in θ_0, due to which the difference between two complex vectors phases must be zero. The term inside the real part operator $\Re e\{\cdot\}$ is the most important and it basically determines the shape of the Array Factor. It can be straightforwardly shown that, depending on the value of ϕ_2 and ϕ_3, the MRD θ_{max} and the direction of the main secondary lobe θ_{msl} are located in either two points, corresponding to the directions for which the complex exponential is 1 or -1. Introducing the angles:

$$\chi = arcsin\left(sin(\theta_0) - \frac{\phi_3}{2\pi} - 2m\right) \quad (4a)$$

$$\psi = arcsin\left(sin(\theta_0) - \frac{\phi_3}{2\pi} - (2m+1)\right) \quad (4b)$$

where m is an integer value chosen in order to keep the arcsin argument in its definition domain [-1;1], it is $\theta_{max} = \chi, \theta_{msl} = \psi$ if $cos\left(\phi_2 - \frac{\phi_3}{2}\right) > 0$, while it is $\theta_{max} = \psi$, $\theta_{msl} = \chi$ if $cos\left(\phi_2 - \frac{\phi_3}{2}\right) < 0$. This last result explains how the phase shifts influence the MRD: changing ϕ_3 directly affects θ_{max} and θ_{msl} in any case, while changing ϕ_2 does not affect θ_{max} and θ_{msl}, unless the sign of $cos\left(\phi_2 - \frac{\phi_3}{2}\right)$ is switched.

The tolerance of the system with respect to the phase shifts can be evaluated in terms of deviation of θ_{max} from the desired MRD θ_0, which allows to determine an interval of admittable values for ϕ_3, and in terms of the ratio R between the powers emitted in the main and in the secondary lobe directions (θ_{max} and θ_{msl}, respectively) which allows to determine an interval of admittable values for ϕ_2.

Indeed, defining a maximum deviation θ_{th}, the values of ϕ_3 for which $\theta_{max} = \theta_0 \pm \theta_{th}$, can be determined as:

$$\phi_{3,max}^{+,-} = 2\pi(sin(\theta_0) - sin(\theta_0 \pm \theta_{th})) \quad (5)$$

so that it must be $\phi_3 \in \left[\phi_{3,max}^{-}, \phi_{3,max}^{+}\right]$.

With reference to this result, it can be observed that the values of $\phi_{3,max}^{+,-}$ depend on θ_0. The more θ_0 approaches $\pm 90°$ i.e., the limits of the half-space available for transmission, the lower is the range $\left[\phi_{3,max}^{-}, \phi_{3,max}^{+}\right]$. As mentioned above, the interval of admittable values for ϕ_2 can instead be determined considering the ratio of $|AF_h(\theta,t)|^2$ evaluated in the directions of the main lobe and of the secondary lobe, respectively. Referring, without loss of generality, to the case where $cos\left(\phi_2 - \frac{\phi_3}{2}\right) \geq 0$, the correspondent expression can be obtained from (3) as:

$$R = \frac{|AF_h(\chi,t)|^2}{|AF_h(\psi,t)|^2} = \frac{5 + 4\,cos\left(\phi_2 - \frac{\phi_3}{2}\right)}{5 - 4\,cos\left(\phi_2 - \frac{\phi_3}{2}\right)} \quad (6)$$

where it is $R \in [1,9]$, according to the value of $\left(\phi_2 - \frac{\phi_3}{2}\right)$.

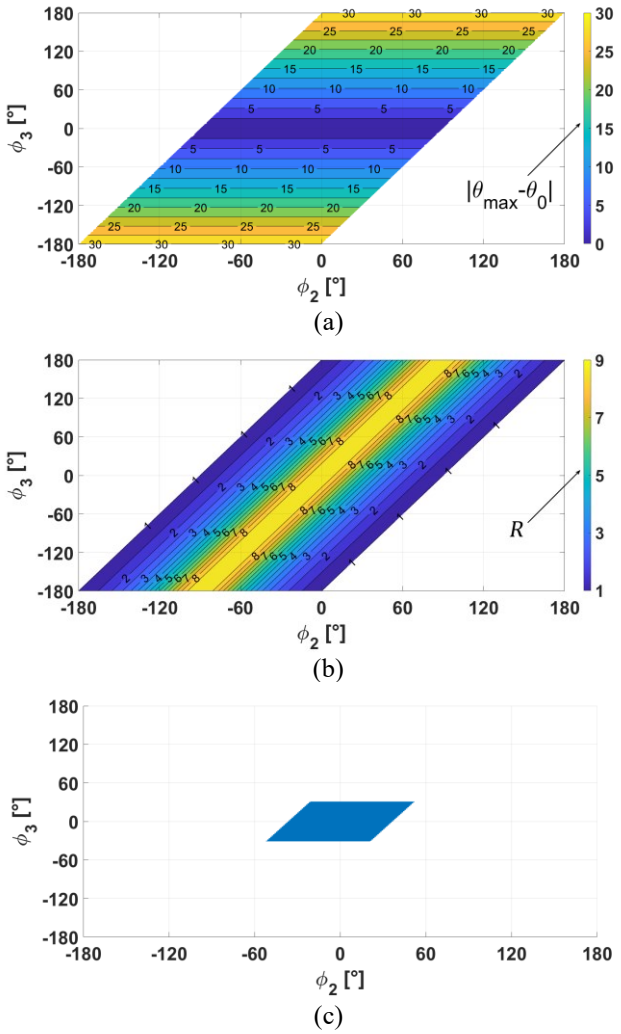

Fig. 3. Contour plots of the surfaces determining the phase shifts tolerance intervals when $\theta_0 = 0°$. (a) is the contour plot of the deviation of θ_{max} from θ_0, given by $|\theta_{max} - \theta_0|$. The domain is limited to values of ϕ_2 and ϕ_3 such that $|\theta_{max} - \theta_0| \in [0°, 30°]$. (b) is the contour plot of the ratio R determined by (6). The domain is limited to values of ϕ_2 and ϕ_3 such that $R \in [1,9]$. (c) is the domain of ϕ_2 and ϕ_3 obtained by intersecting the domains of (a) when $|\theta_{max} - \theta_0| \leq 5°$ and (b) when $R \geq 4.5$.

Choosing for example a value $R \geq 4.5$ as representative for a "good" ratio between main and secondary lobe power level, leads to approximately $\frac{\phi_3}{2} - 37° \leq \phi_2 \leq \frac{\phi_3}{2} + 37°$.

Fig. 3(a) represents the contour plot of the MRD deviation from θ_0 (chosen as θ_0=0°) limited to the maximum value $\theta_{th} = 30°$. It is obtained from (4a) and (4b) by solving for different values of ϕ_2 and ϕ_3, thus finding θ_{max} and then computing $|\theta_{max} - \theta_0|$. Fig. 3(b) represents instead the contour plot surface described by (6), again when θ_0=0°. In particular, the domain of interest for Fig. 3(b) is for values of (6) greater than 1. In Fig. 3(c) the intersection of the domains of the two previous surfaces is given: it represents the interval of tolerable values of ϕ_2 and ϕ_3, for which the MRD deviation is less than or equal to 5° and $R \geq 4.5$, and is shaped as a parallelogram.

The situation represented in Fig. 3, related to the Radiation Diagram emitted at carrier frequency f_0 by the TMA described in experimental part of this work (see Fig. 5(a)), has to be

intended as an explicative example that shows how to find the intervals of tolerable phase shifts ϕ_2 and ϕ_3 for fixed values of θ_0, θ_{th} and R. Once that the modulating sequences are chosen, the described procedure must be applied to all frequencies of interest irradiated by the TMA, obtaining a parallelogram-shaped domain for each of them. The intersection of all the domains gives the common tolerance intervals of ϕ_2 and ϕ_3 to all frequencies of interest. This operation is going to be performed in the following Section.

III. Experimental Results and Comparison

The experimental set-up adopted to verify the previous analyses is shown in Fig. 4 and results composed of a RoF link followed by a 3-element antenna array. The low number of radiating elements assures cost effectiveness and reduced space occupancy, making this solution attractive for indoor SoHo scenarios, as mentioned in the Introduction.

The RoF system consists of an Optical Transmitter based on a directly modulated DFB laser, followed by 1 km of single mode G652 optical fiber, and by a 1:3 optical splitter, ending in three Optical Receivers based on PIN photodetectors followed by a RF amplifier. The RoF system is followed by a linear TMA, made by three square patch antennas realized on Rogers RO4350B (thickness: 1.524 mm, with ε_r=3.48, tan(δ)=0.0037), resonating at 2.45 GHz, separated by 61 mm (about half wavelength in free-space), and with a maximum gain of 4 dBi [30]. Despite 5G array antennas are mostly operating in the upper K-band, the proposed solution exploits the Industrial, Scientific and Medical (ISM) band to demonstrate the RoF/TMA fruitful coexistence within an operation bandwidth of application interest. However, the scaling of the system to millimetre frequency is feasible: optical transmitters and receivers with appropriate RF bandwidths should in this case be employed, to guarantee that the TMA piloting devices are able to work in the K-band, still maintaining the same switching frequency [31] [32].

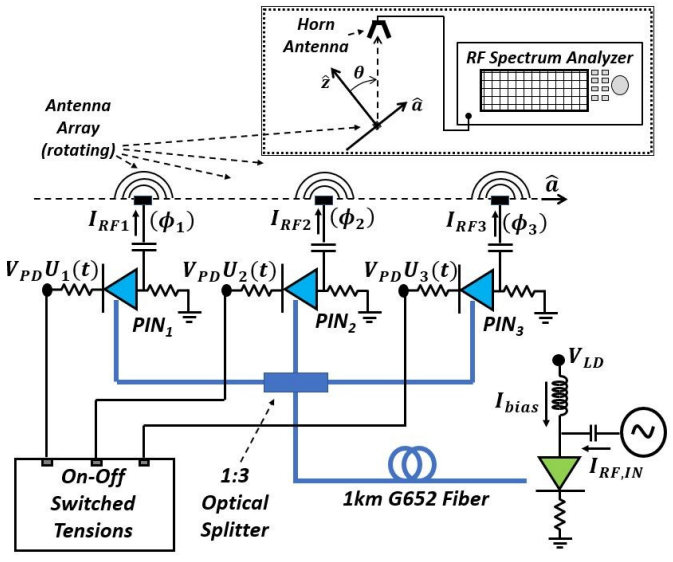

Fig. 4 Experimental setup of the RoF-TMA system studied. V_{LD}, I_{bias}, $I_{RF,IN}$: direct bias voltage, direct bias current and RF modulating current of the laser diode, respectively. Letting n = 1,2,3 it is: $V_{PD}, U_n(t)$: respectively reverse bias voltage and modulating sequence of photodiode PIN_n ; $I_{RF,n}$: input RF signal feeding the $n-th$ antenna, with phase ϕ_n.
Inset: radiation pattern evaluation.

The DFB laser operates in the second optical window (wavelength λ~1310 nm), has slope efficiency $\eta = 0.08\ W/A$ and modulation bandwidth ranging from 10 MHz to around 3.5 GHz. Its 1 dB input compression point and third order input intercept point are $P_{1dB} = 20\ dBm$ and $P_{IIP3} = 33\ dBm$, respectively. Each RoF branch that feeds the single patch antenna exhibits a RF Gain of about -23.5dB in the bandwidth of interest and same P_{1dB}, P_{IIP3} as the ones of the laser, guaranteeing the correct operation of the analog optical link [33].

Through an evaluation board *STM32VLDiscovery*, time-varying tensions $V_{PD}U_n(t)$ are generated, where V_{PD} is the DC reverse voltage of each one of the PINs. The sequences $U_n(t)$ present a modulation frequency $f_M = 10\ kHz$, duty cycles $c_n = 80\%$ and initial delays $c_{i,n}$ equal to 0%, 33% and 66% for n = 1,2,3, respectively. When $U_n(t) = 0$, the $n-th$ photodetector is not reversely biased, and its Responsivity at 2.45GHz is very low, so that the modulating component of the optical power at 2.45GHz is practically not detected. Thus, in that time period, the level of the RF signal current I_{RFn} which goes to the antenna is zero. On the contrary, when $U_n(t) = 1$ the level of the reverse biasing voltage is $V_{PD} = -1.5V$, and the response of the RoF link at 2.45 GHz increases by about 34 dB with respect to the previous case, so that the RF component which modulates the optical power can be detected and the current I_{RFn} can travel toward the $n-th$ antenna with amplitude not zero.

It is worth noticing that the chosen sequences do not correspond to the optimum exploitation of the TMA sideband radiation as multi-direction beam launcher (e.g. the maxima of radiation at frequencies $f_0 + hf_M$ result lower than the one at f_0), but represent just a significant example on which the theoretical considerations exposed in this work are taken.

As shown in Fig. 4, the radiation diagram is then evaluated by rotating the 3-antenna array from -90° to 90° and receiving the power emitted with a fixed TDK horn antenna directly connected to a spectrum analyser, which performs the measurement of the power of each harmonic $f_0 + hf_M$ considered. The analysed frequencies range from f_0 to $f_0 + 4f_M$. The quality factor R expressed by (6) is chosen to be 4.5, while the angle shift tolerance θ_{th} is set to 5°.

Fig. 5(a) shows the ideal squared Array Factor $|AF_h(\theta,t)|^2$, normalized to the maximum value, obtained by applying the test sequence, while Tab. 1 summarizes the different MRD and $\phi_{3,max}^{+,-}$ of each harmonic. In order to satisfy the constraint (5) for every frequency, ϕ_3 must be $-25.2° \le \phi_3 \le 24.9°$.

The antenna currents present inherent phase shifts ϕ_n deriving from the splitter, which can be changed by putting additional strands of fiber to the corresponding splitter outputs. In this way, it is possible to measure the received radiation pattern in different phase shifts conditions. In particular, three different cases are taken into account: ϕ_2 or ϕ_3 out of their range of tolerance and the phase shifts in the range of tolerance. As described previously, any change in ϕ_3 directly affects the MRD, while only significant changes in ϕ_2 can modify the MRD.

Each set of measurements is paired with a Matlab simulation of the Radiation Diagram of the TMA. This simulation is a

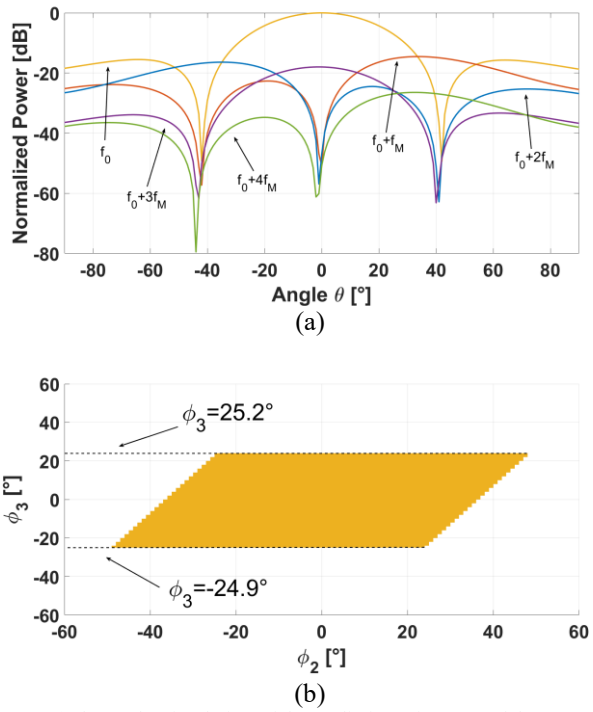

Fig. 5. (a) shows the simulation of the Radiation Diagrams of the TMA when fed with the test modulating sequences, at frequencies ranging from f_0 to $f_0 + 4f_M$ and normalized to the maximum radiated power at f_0. Each curve is obtained by multiplying $|AF_h(\theta,t)|^2$, given by (3), with the absolute squared far-field radiated by the single antenna (i.e. the Element Factor). Each color is related to a frequency: yellow to f_0, red to $f_0 + f_M$, blue to $f_0 + 2f_M$, purple to $f_0 + 3f_M$ and green to $f_0 + 4f_M$. (b) shows the intersection of the phase shift domains related to the frequencies of interest, represented by the yellow area. The single domains were obtained by considering $|\theta_{max} - \theta_0| \leq |\theta_{th}| = 5°$ and $R \geq 4.5$.

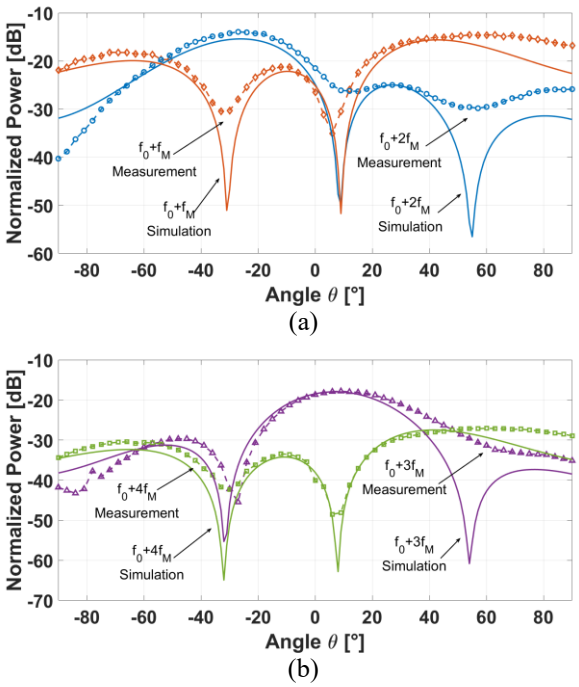

Fig. 6. Simulated (continuous line) and measured (dashed line with markers) received Radiation Diagrams for the first scenario. (a) shows frequencies $f_0 + f_M$ (red with diamond markers) and $f_0 + 2f_M$ (blue with circle markers). (b) shows frequencies $f_0 + 3f_M$ (purple with triangle markers) and $f_0 + 4f_M$ (green with square markers). The power values of the simulations and of the measurements are normalized to the respective maximum radiated power at frequency f_0.

h	θ_0	$\phi_{3,max}^{+}$	$\phi_{3,max}^{-}$
1	34°	26.8°	-25.2°
2	-35°	24.9°	-26.5°
3	-1°	31.3°	-31.4°
4	33°	27.1°	-25.6°

Tab. 1. Values of the desired MRD θ_0 and of the maximum and minimum allowed phase shift ϕ_3 for each frequency $f_0 + hf_M$ related to the test modulating sequences when the phase shifts are all 0°.

h	Measured θ_{max}	Simulated χ	Simulated ψ
1	63°	55.5°	-10°
2	-27°	-31°	29°
3	9°	8°	-59°
4	60°	53.5°	-11.5°

Tab. 2. Values of the measured MRD θ_{max} and of the simulated χ and ψ directions for each frequency $f_0 + hf_M$ related to the first scenario. In this scenario, the direction χ corresponds to the main lobe direction, while ψ to the secondary lobe direction, due to $cos\left(\phi_2 - \frac{\phi_3}{2}\right) > 0$. The value of ϕ_3 exceeds the limits fixed in Tab. 1, while ϕ_2 is such that $R > 4.5$ for all frequencies. The values of θ_{max} and χ result to be all shifted of more than 5° (i.e. θ_{th}) with respect to the values of θ_0 in Tab. 1.

direct application of the array factor formula shown in (3) multiplied by the absolute squared far-field emitted by the single antenna, i.e., the Element Factor. The single element behavior is modeled as an omnidirectional antenna for θ ranging from -90° to 90°, with greater directivity in the broadside area, as confirmed also by experimental measurements.

A. First scenario: ϕ_3 out of the range of tolerance

In this scenario, the phase shifts $\phi_2 = 31.2°$ and $\phi_3 = 58.6°$ are imposed to the system. In this case, only ϕ_3 is out of the tolerance range, as the interval for ϕ_2 is bounded by $\frac{\phi_3}{2} + 37° = 66.3°$ and $\frac{\phi_3}{2} - 37° = -7.7°$, while ϕ_3 is above the maximum upper bound $\phi_{3,max}^{+}$=31.3° in Tab. 1. Consequently, the MRDs at all frequencies under test are expected to be shifted of more than the tolerance value $\theta_{th} = 5°$.

The resulting simulations and measurements are shown in Tab. 2 and Fig. 6. The plots depict the comparison between simulation (continuous lines) and measurement (dashed line with marker) and are organized in two distinct figures for clarity. In particular, Fig. 6(a) is related to frequencies $f_0 + f_M$ and $f_0 + 2f_M$, while Fig. 6(b) to $f_0 + 3f_M$ and $f_0 + 4f_M$. All the radiation diagrams are normalized with respect to the maximum received power at f_0. Tab. 2 shows the measured MRD along with the directions χ and ψ, obtained with (4a) and (4b) and confirmed by the simulation curves. In this case, χ is the main lobe direction, while ψ is the secondary lobe direction, due to $cos\left(\phi_2 - \frac{\phi_3}{2}\right) > 0$. This is confirmed by considering that the

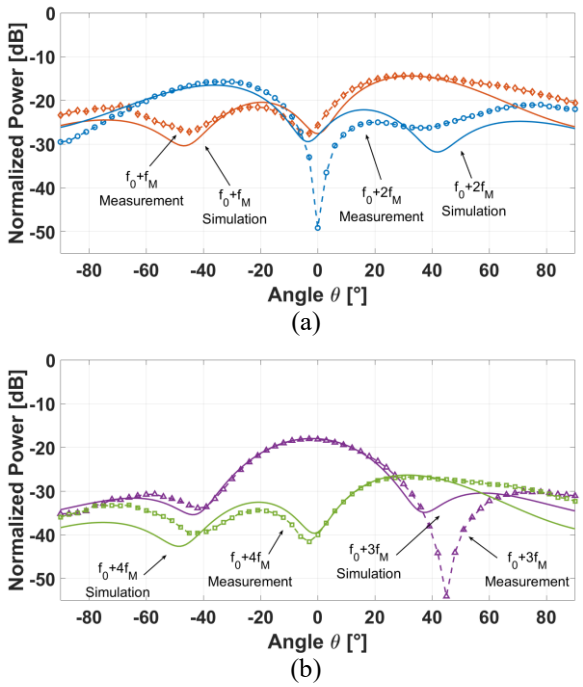

Fig. 7. Simulated (continuous line) and measured (dashed line with markers) received Radiation Diagrams for the second scenario. (a) shows frequencies $f_0 + f_M$ (red with diamond markers) and $f_0 + 2f_M$ (blue with circle markers). (b) shows frequencies $f_0 + 3f_M$ (purple with triangle markers) and $f_0 + 4f_M$ (green with square markers). The power values of the simulations and of the measurements are normalized to the respective maximum radiated power at frequency f_0.

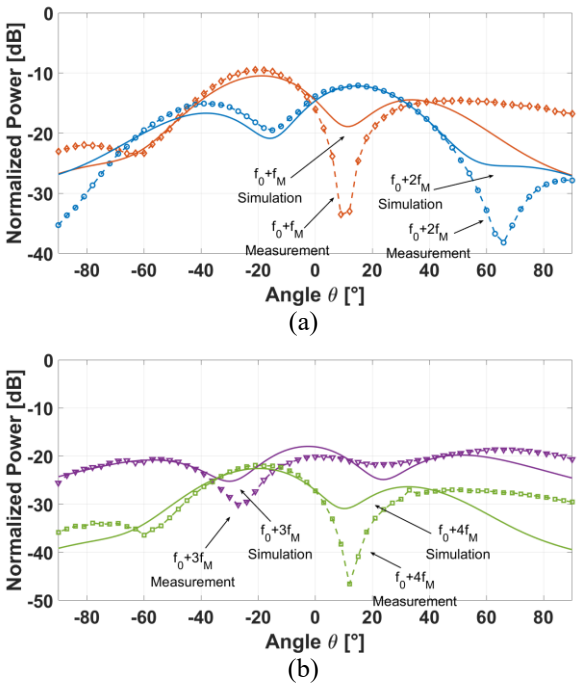

Fig. 8. Simulated (continuous line) and measured (dashed line with markers) received Radiation Diagrams for the third scenario. (a) shows frequencies $f_0 + f_M$ (red with diamond markers) and $f_0 + 2f_M$ (blue with circle markers). (b) shows frequencies $f_0 + 3f_M$ (purple with triangle markers) and $f_0 + 4f_M$ (green with square markers). The power values of the simulations and of the measurements are normalized to the respective maximum radiated power at frequency f_0.

h	Measured θ_{max}	Simulated χ	Simulated ψ
1	-21°	39.5°	-21.5°
2	15°	-45°	17°
3	63°	-2.5°	72.5°
4	-21°	38°	-23°

Tab. 3. Values of the measured MRD θ_{max} and of the simulated χ and ψ directions for each frequency $f_0 + hf_M$ related to the second scenario. In this scenario, the direction ψ corresponds to the main lobe direction, while χ to the secondary lobe direction, due to $cos\left(\phi_2 - \frac{\phi_3}{2}\right) < 0$. The value of ϕ_3 is inside the limits fixed in Tab. 1, while ϕ_2 is such that $R < 4.5$ for all frequencies. The values of θ_{max} and ψ are all shifted of more than 5° (i.e. θ_{th}) with respect to the values of θ_0 in Tab. 1.

h	Measured θ_{max}	Simulated χ	Simulated ψ
1	30°	40°	-21°
2	-30°	-44.5°	17.5°
3	-3°	-2.5°	73.5°
4	33°	38.5°	-22.5°

Tab. 4. Values of the measured MRD θ_{max} and of the simulated χ and ψ directions for each frequency $f_0 + hf_M$ related to the third scenario. In this scenario, the direction χ corresponds to the main lobe direction, while ψ to the secondary lobe direction, due to $cos\left(\phi_2 - \frac{\phi_3}{2}\right) > 0$. The value of ϕ_3 is inside the limits fixed in Tab. 1, while ϕ_2 is such that $R > 4.5$ for all frequencies. The values of θ_{max} and χ are all shifted of less than 5° (i.e. θ_{th}) with respect to the values of θ_0 in Tab. 1.

values of the measured MRD are closer to the values of χ. The measurements are in good accordance with the simulations and the MRDs are shifted of more than 5°, as shown by comparing θ_{max} in Tab. 2 with θ_0 in Tab. 1.

B. Second scenario: ϕ_2 out of the range of tolerance

In this scenario, the applied phase shifts are $\phi_2 = 106.6°$ and $\phi_3 = -10.2°$. In this case, ϕ_3 is in its range of tolerance between -25.2° and 24.9° and only ϕ_2 is out of its range of tolerance, which is between -42.1° and 31.9°. It has to be noted that it also exceeds the limit value $\frac{\phi_3}{2} + 90° = 84.9°$, meaning that the MRD is actually located in ψ (from (4b)). In Tab. 3 and Fig. 7, simulations and measurements, normalized to the maximum received power at f_0, are compared as in the previous case, with Fig. 7(a) related to $f_0 + f_M$ and $f_0 + 2f_M$ and Fig. 7(b) to $f_0 + 3f_M$ and $f_0 + 4f_M$, while Tab. 3 is the equivalent of Tab. 2 for this scenario. The measurements are compliant with the simulations and the results match with the expectations. In particular, even if ϕ_3 is in the range of tolerance, the MRD is not located in χ but in ψ, due to $cos\left(\phi_2 - \frac{\phi_3}{2}\right) < 0$. This is confirmed by Tab. 3, where the measured θ_{max} is closer to the simulated ψ and shifted of more than 5° when compared to θ_0 in Tab. 1. As an additional effect, the side lobe level and the extinction ratio (ratio between highest and lowest value) of the radiation diagrams result to be degraded compared to the ideal case.

C. Third scenario: ϕ_2 and ϕ_3 in the range of tolerance

In the last scenario, the phase shifts $\phi_2 = -34.8°$ and $\phi_3 = -7.4°$ are applied to the TMA. These phases are within the intervals of tolerance $-40.7° \leq \phi_2 \leq 33.3°$ and $-25.2° \leq \phi_3 \leq 24.9°$ and ensure that the MRD are not shifted of more than 5°. The simulated and measured received Radiation Diagrams, shown in Fig. 8, are in agreement, showing that there is only a slight degradation in the side lobe level due to ϕ_2. The information in Tab. 4 is compliant with the expectations, showing that the MRD is located in χ instead of ψ and that the deviation from θ_0 in Tab. 1 is less than 5°.

In all the exposed cases, the measurements are in good agreement with the simulations in both radiation direction and level, confirming the correctness of the theoretical predicted impact of ϕ_2 and ϕ_3 on the TMA response given by the conditions (5) and (6) shown in Section II. Inaccuracies are present in some of the measurements, especially regarding the depth of the minima directions or the level at +90° and -90°, mainly due to the real environment where they are carried out. However, their impact in the overall behavior of the TMA is small and there are no major anomalies that need to be discussed, thus confirming the model developed in this work.

IV. Conclusion

Through a detailed theoretical and experimental analysis the feasibility of a cost-efficient system for the distribution of the wireless signal within in-building environments which combines the techniques of Radio over Fiber (RoF) and Time Modulation of Antenna Arrays (TMA) is demonstrated.

With reference to the applicative case considered it has been found that a 3-element TMA, in the frequencies ranging from $f_0 + f_M$ to $f_0 + 4f_M$, each with a MRD between $-35°$ and $+35°$, can tolerate a phase shift ϕ_3 in the interval $-25.2° \leq \phi_3 \leq 24.9°$ and a phase shift ϕ_2 in the interval $\frac{\phi_3}{2} - 37° \leq \phi_2 \leq \frac{\phi_3}{2} + 37°$. At the considered frequency, being the refractive index of the fiber around 1.47, the length of fiber associated to the deviation of ϕ_3 is equal to ± 5.8 mm. A maximum tolerable difference between the different paths of the splitter equal to this quantity represents a fabrication constraint which is fairly easy to fulfill.

Higher precision levels would however be required if the highest frequencies of the 5G spectrum were involved.

Further investigations on the exploitation of the presented results to larger arrays have demonstrated the effectiveness of the method: from a practical point of view, the satisfaction of the phase-conditions (5) and (6) for the first three antennas (thus involving ϕ_2 and ϕ_3, only) of a four- or five-element array gives the possibility to easily and rapidly select the remaining phases (ϕ_4 and/or ϕ_5) in such a way to satisfy the maxima and side-lobe levels conditions of the multi-harmonic radiation.

Appendix

A. Equation (2) derivation

In previous works such as [23], u_{hn} has two expressions, one if $0 \leq c_{i,n} \leq (1 - c_n)$ and the other if $(1 - c_n) < c_{i,n} \leq 1$. The following demonstrates that there is no need to make a distinction between the two cases. If $c_{i,n}$ is the rising instant, $c_{f,n}$ the falling instant and c_n is the duty cycle, the first case $0 \leq c_{i,n} \leq (1 - c_n)$ implies that $c_{f,n} \geq c_{i,n}$ and $c_n = c_{f,n} - c_{i,n}$ and u_{hn} is

$$\begin{aligned} u_{hn} &= \frac{1}{T_M}\int_0^{T_M} U_n(t) e^{-j2\pi h f_M t} dt \\ &= \frac{1}{T_M}\int_{c_{i,n}T_M}^{c_{f,n}T_M} e^{-j2\pi h f_M t} dt \\ &= \frac{e^{-j2\pi h c_{i,n}} - e^{-j2\pi h c_{f,n}}}{j2\pi h} \\ &= e^{-j\pi h(c_n + 2c_{i,n})} \frac{e^{j\pi h c_n} - e^{-j\pi h\left(2c_{f,n} - 2c_{i,n} - c_n\right)}}{j2\pi h} \\ &= c_n e^{-j\pi h(c_n + 2c_{i,n})} \frac{e^{j\pi h c_n} - e^{-j\pi h c_n}}{j2\pi h c_n} \\ &= c_n sinc(h\pi c_n) e^{-jh\pi(c_n - 2c_{i,n})} \end{aligned} \tag{8}$$

It was implied in the solution of the integral that $e^{-j2\pi h} = 1$, since h is an integer coefficient. While the second case $(1 - c_n) < c_{i,n} \leq 1$ implies that $c_{f,n} \leq c_{i,n}$ and $c_n = 1 - \left(c_{i,n} - c_{f,n}\right)$ and u_{hn} is

$$\begin{aligned} &u_{hn} \\ &= \frac{1}{T_M}\left(\int_0^{c_{f,n}T_M} e^{-j2\pi h f_M t} dt + \int_{c_{i,n}T_M}^{T_M} e^{-j2\pi h f_M t} dt\right) \\ &= \frac{e^{-j2\pi h c_{i,n}} - e^{-j2\pi h c_{f,n}}}{j2\pi h} \\ &= e^{-j\pi h(c_n + 2c_{i,n})} \frac{e^{j\pi h c_n} - e^{-j\pi h\left(2c_{f,n} - 2c_{i,n} - c_n + 2 - 2\right)}}{j2\pi h} \\ &= c_n e^{-j\pi h(c_n + 2c_{i,n})} \frac{e^{j\pi h c_n} - e^{-j\pi h c_n} e^{j2\pi h}}{j2\pi h c_n} \\ &= c_n sinc(h\pi c_n) e^{-jh\pi(c_n - 2c_{i,n})} \end{aligned} \tag{9}$$

Thus demonstrating the equivalence of the two cases.

B. Phase alignment condition

The phase alignment in θ_0 in the assumptions, requires that the complex vectors phases in (1) satisfy

$$\begin{cases} \langle u_{h1} = \langle u_{h2} + kd\ sin(\theta_0) + 2\pi m_1 \\ \langle u_{h1} = \langle u_{h3} + 2kd\ sin(\theta_0) + 2\pi m_2 \\ \langle u_{h2} + kd\ sin(\theta_0) = \langle u_{h3} + 2kd\ sin(\theta_0) + 2\pi m_3 \end{cases} \downarrow$$

$$\begin{cases} h\pi(c_1 - c_2 + 2c_{i,2} - 2c_{i,1}) = kd\ sin(\theta_0) + 2\pi m_1 \\ h\pi(c_1 - c_3 + 2c_{i,3} - 2c_{i,1}) = 2kd\ sin(\theta_0) + 2\pi m_2 \\ h\pi(c_2 - c_3 + 2c_{i,3} - 2c_{i,2}) = kd\ sin(\theta_0) + 2\pi m_3 \end{cases} \downarrow \quad (10)$$

$$\begin{cases} sin(\theta_0) = -2hc_{i,2} + 2m_1 \\ sin(\theta_0) = -hc_{i,3} + m_2 \\ sin(\theta_0) = 2h(c_{i,2} - c_{i,3}) + 2m_3 \end{cases} \downarrow$$

$$\begin{cases} sin(\theta_0) = -2hc_{i,2} + 2m_1 \\ h(2c_{i,2} - c_{i,3}) = 2m_1 - m_2 \\ h(2c_{i,2} - c_{i,3}) = m_2 - 2m_3 \end{cases}$$

where m_1, m_2 and m_3 are integer coefficients added to account for the phases 2π periodicity. The system is formed by equalling pairs of vectors phases from Eq. 1. From the 2nd and 3rd equations in the final system, the condition $h(2c_{i,2} - c_{i,3}) \in \mathbb{Z}$ is necessary to have phase alignment, since h, m_1, m_2 and m_3 are already integer quantities. To be noted that if $(2c_{i,2} - c_{i,3}) \in \mathbb{Z}$, then the phase alignment is guaranteed for all frequencies $f_0 + hf_M$, while in the general case only some values of h satisfy the condition since $c_{i,2}$ and $c_{i,3}$ are fixed a priori.

C. Equation (3) derivation

The following property of complex numbers is exploited to derive the final expression of (3):

$$|C_1 + C_2 + C_3|^2 = |C_1|^2 + |C_2|^2 + |C_3|^2 + 2\Re e\{C_1C_2^* + C_2C_3^* + C_1C_3^*\} \quad (11)$$

with C_1, C_2 and C_3 being complex numbers. Equation (11) along with the phase alignment condition is then applied to (3) as it can be seen in (12) in the footnote.

REFERENCES

[1] A. Osseiran et. al, "5G wireless access: an overview", Ericsson White Paper, 2020 . [Online]. Available: https://www.ericsson.com/en/reports-and-papers/white-papers/5g-wireless-access-an-overview

[2] K. Chandra, et al, "CogCell: cognitive interplay between 60 GHz picocells and 2.4/5 GHz hotspots in the 5G era," *IEEE Comm. Mag.,* vol. 53, no. 7, pp. 118–125, Jul. 2015,

[3] N. Wang, E. Hossain and V. K. Bhargava, "Backhauling 5G small cells: A radio resource management perspective," in IEEE Wireless Communications, vol. 22, no. 5, pp. 41-49, October 2015.

[4] T. Chen, M. B. Dastjerdi, H. Krishnaswamy and G. Zussman, "Wideband Full-Duplex Phased Array With Joint Transmit and Receive Beamforming: Optimization and Rate Gains," in IEEE/ACM Transactions on Networking.

[5] D. Belo, D. C. Ribeiro, P. Pinho and N. Borges Carvalho, "A Selective, Tracking, and Power Adaptive Far-Field Wireless Power Transfer System," in IEEE Transactions on Microwave Theory and Techniques, vol. 67, no. 9, pp. 3856-3866, Sept. 2019.

[6] M. Del Prete, D. Masotti, N. Arbizzani and A. Costanzo, "Remotely Identify and Detect by a Compact Reader With Mono-Pulse Scanning Capabilities," *IEEE Trans. Microw. Th. Techn.*, vol. 61, no. 1, pp. 641-650, Jan. 2013, doi: 10.1109/TMTT.2012.2229290BD

[7] J. G. Lee, T. H. Jang, G. H. Park, H. S. Lee, C. W. Byeon and C. S. Park, "A 60-GHz Four-Element Beam-Tapering Phased-Array Transmitter With a Phase-Compensated VGA in 65-nm CMOS," *IEEE Trans. Microw. Th. Techn.*, vol. 67, no. 7, pp. 2998-3009, July 2019, doi: 10.1109/TMTT.2019.2907242.

[8] W. H. Kummer, et al, "Ultra-low sidelobes from time-modulated arrays," *IEEE Trans. Ant. Prop.*, vol. AP-11, no. 6, pp. 633-639, Nov. 1963, doi: 10.1109/TAP.1963.1138102.

[9] D. Masotti and A. Costanzo, "Time-based RF showers for energy-aware power transmission," 2017 11th European Conference on Antennas and Propagation (EUCAP), Paris, France, 2017, pp. 783-787, doi: 10.23919/EuCAP.2017.7928158.

[10] A. Giovannini et al., "Radio over Fiber–driven Time Modulated Array Antennas for Efficient Beamforming within In-Building Environments," 2020 European Conference on Optical Communications (ECOC), Brussels, Belgium, 2020, pp. 1-4, doi: 10.1109/ECOC48923.2020.9333311

[11] A. Giovannini et al., "Beam-Steering Features of Radio-over-Fiber Systems via Antenna Array Time Modulation," 2020 International Topical Meeting on Microwave Photonics (MWP), Matsue, Japan, 2020, pp. 140-143, doi: 10.23919/MWP48676.2020.9314581.

[12] J. Nanni et al., "Optimum Mitigation of distortion induced by Rayleigh Backscattering in Radio-over-Fiber links for the Square Kilometer Array Radio-Telescope," 2019 International Topical Meeting on Microwave Photonics (MWP), 2019, pp. 1-4

[13] D. Wake, A. Nkansah and N. J. Gomes, "Radio Over Fiber Link Design for Next Generation Wireless Systems," in Journal of Lightwave Technology, vol. 28, no. 16, pp. 2456-2464, Aug.15, 2010.

[14] J. Nanni et al, "VCSEL-Based Radio-Over-G652 Fiber System for Short-/Medium Range MFH Solutions," IEEE/OSA J. Lightw. Technol, vol. 36, pp. 4430-4437, Oct.1, 2018.

[15] J. Nanni, et al, "VCSEL-SSMF-based Radio-over-Fiber link for low cost and low consumption wireless dense networks," Proc. Int. Topical Meeting Microw. Photonics (MWP), Beijing, Oct. 2017.

[16] Y. Shi et al., "Ultrawideband Signal Distribution Over Large-Core POF for In-Home Networks," IEEE/OSA J. Lightw. Technol, vol. 30, pp. 2995-3002, Sept. 2012.

$$\begin{aligned} &|AF_h(\theta,t)|^2 = \\ &|AC\ sinc(h\pi C)|^2\left(3 + 2\Re e\left\{e^{j(-2h\pi c_{i,2} - \pi\ sin(\theta) - \phi_2)} + e^{j(2h\pi(c_{i,2} - c_{i,3}) - \pi\ sin(\theta) + \phi_2 - \phi_3)} + e^{j(-2h\pi c_{i,3} - 2\pi\ sin(\theta) - \phi_3)}\right\}\right) = \\ &|AC\ sinc(h\pi C)|^2\left(3 + 2\Re e\left\{e^{j(\pi\ sin(\theta_0) - \pi\ sin(\theta) - \phi_2)} + e^{j(\pi\ sin(\theta_0) - \pi\ sin(\theta) + \phi_2 - \phi_3)} + e^{j(2\pi\ sin(\theta_0) - 2\pi\ sin(\theta) - \phi_3)}\right\}\right) = \\ &|AC\ sinc(h\pi C)|^2\left(3 + 2\Re e\left\{e^{j\left(\pi\ sin(\theta_0) - \pi\ sin(\theta) - \frac{\phi_3}{2}\right)}\left(\left(e^{-j\left(\phi_2 - \frac{\phi_3}{2}\right)} + e^{j\left(\phi_2 - \frac{\phi_3}{2}\right)}\right) + e^{j\left(\pi\ sin(\theta_0) - \pi\ sin(\theta) - \frac{\phi_3}{2}\right)}\right)\right\}\right) = \\ &= |AC\ sinc(h\pi C)|^2\left(3 + 2\Re e\left\{e^{j\left(\pi\ sin(\theta_0) - \pi\ sin(\theta) - \frac{\phi_3}{2}\right)}\left(2cos\left(\phi_2 - \frac{\phi_3}{2}\right) + e^{j\left(\pi\ sin(\theta_0) - \pi\ sin(\theta) - \frac{\phi_3}{2}\right)}\right)\right\}\right) \end{aligned} \quad (12)$$

[17] D. Visani et al, "Link Design Rules for Cost-Effective Short-Range Radio Over Multimode Fiber Systems," IEEE Trans. Microw. Theory Techn., vol. 58, pp. 3144-3153, Nov. 2010.
[18] J. Nanni et al., "Use of SiGe Photo-Transistor in RoF links based on VCSEL and standard single mode fiber for low cost LTE applications," 2018 International Topical Meeting on Microwave Photonics (MWP), Toulouse, France, 2018, pp. 1-4, doi: 10.1109/MWP.2018.8552865.
[19] J. Nanni, J. Polleux, C. Algani, S. Rusticelli, F. Perini and G. Tartarini, "Chirp Evaluation of 850-nm Single Mode VCSEL Exploiting Modal Noise in Standard Single Mode Fiber," in IEEE Journal of Quantum Electronics, vol. 54, no. 4, pp. 1-11, Aug. 2018, Art no. 2400611, doi: 10.1109/JQE.2018.2855204.
[20] J. Nanni et al., "Modal noise in 850nm VCSEL-based radio over fiber systems for manifold applications," 2015 Fotonica AEIT Italian Conference on Photonics Technologies, Turin, 2015, pp. 1-4, doi:10.1049/cp.2015.0112.
[21] J. Nanni et al., "SiGe Photo-Transistor for Low-Cost SSMF-Based Radio-Over-Fiber Applications at 850nm," *IEEE Journ. of Quant.Electr.,* vol. 55, no. 4, pp. 1-9, Aug. 2019, Art no. 4600109, doi: 10.1109/JQE.2019.2917209.
[22] D. Masotti, A. Costanzo, M. Del Prete and V. Rizzoli, "Time-Modulation of Linear Arrays for Real-Time Reconfigurable Wireless Power Transmission," in *IEEE Transactions on Microwave Theory and Techniques*, vol. 64, no. 2, pp. 331-342, Feb. 2016, doi: 10.1109/TMTT.2015.2512275.
[23] L. Poli, P. Rocca, G. Oliveri and A. Massa, "Harmonic Beamforming in Time-Modulated Linear Arrays," in *IEEE Transactions on Antennas and Propagation*, vol. 59, no. 7, pp. 2538-2545, July 2011, doi: 10.1109/TAP.2011.2152323.
[24] Y. Tong and A. Tennant, "Simultaneous control of sidelobe level and harmonic beam steering in time-modulated linear arrays," *Electron. Lett.,* vol. 46, no. 3, pp. 201–202, Feb. 2010, doi: 10.1049/el.2010.2629.
[25] G. Li, S. Yang, and Z. Nie, "Direction of arrival estimation in time modulated antenna arrays with unidirectional phase center motion," *IEEE Trans. Antennas Propag.*, vol. 58, no. 4, pp. 1105–1111, Apr. 2010, doi: 10.1109/TAP.2010.2041313.
[26] S. Yang, Y. B. Gan, A. Qing, and P. K. Tan, "Design of a uniform amplitude time-modulated linear array with optimized time sequences," IEEE Trans. Antennas Propag., vol. 53, no. 7, pp. 2337–2339, Jul. 2005.
[27] Q. Zhu, S. Yang, L. Zheng, and Z. Nie, "Design of a low sidelobe time modulated linear array with uniform amplitude and sub-sectional optimized time steps," IEEE Trans. Antennas Propag., vol. 60, no. 9, pp. 4436–4439, Sep. 2012.
[28] L. Poli, P. Rocca, L. Manica, and A. Massa, "Pattern synthesis in time-modulated linear arrays through pulse shifting," *IET Microw., Antennas Propag.,* vol. 4, no. 9, pp. 1157–1164, Sep. 2010, doi: 10.1049/iet-map.2009.0042.
[29] L. Poli, D. Masotti, M. A. Hannan, A. Costanzo and P. Rocca, "Codesign of Switching Sequence and Diode Parameters for Multiple Pattern Optimization in Time-Modulated Arrays," *IEEE Ant. Wirel. Propag. Lett.*, vol. 19, no. 11, pp. 1852-1856, Nov. 2020, doi: 10.1109/LAWP.2020.3010824.
[30] G. Paolini, M. Shanawani, A. Costanzo, F. Benassi and D. Masotti, "RF Energy On-Demand for Automotive Applications," 2020 IEEE/MTT-S International Microwave Symposium (IMS), 2020, pp. 1191-1194, doi: 10.1109/IMS30576.2020.9224078.
[31] Y. Yashchyshyn, K. Derzakowski, P. R. Bajurko, J. Marczewski and S. Kozłowski, "Time-Modulated Reconfigurable Antenna Based on Integrated S-PIN Diodes for mm-Wave Communication Systems," in IEEE Transactions on Antennas and Propagation, vol. 63, no. 9, pp. 4121-4131, Sept. 2015, doi: 10.1109/TAP.2015.2444425.
[32] M. Shanawani, D. Masotti, M. Aldrigo, F. Mastri and A. Costanzo, "Millimeter Wave Agile Transmitter for IoT Operations," 2018 IEEE Wireless Power Transfer Conference (WPTC), 2018, pp. 1-4, doi: 10.1109/WPT.2018.8639322.
[33] C. H. Cox, III, Analog Optical Links: Theory and Practice. Cambridge: Cambridge University Press, 2004.